

<https://doi.org/10.1038/s42004-025-01407-3>

# Real-time visualisation of fast nanoscale processes during liquid reagent mixing by liquid cell transmission electron microscopy



Govind Ummethala<sup>1,2</sup>, Ravi Jada<sup>3</sup>, Shourya Dutta-Gupta<sup>1</sup>, Junbeom Park<sup>4</sup>, Amir H. Tavabi<sup>2</sup>, Shibabrata Basak<sup>4</sup>, Robert Hooley<sup>5</sup>, Hongyu Sun<sup>6</sup>, H. Hugo Pérez Garza<sup>6</sup>, Rüdiger-A Eichel<sup>4</sup>, Rafal E. Dunin-Borkowski<sup>2</sup>✉ & Sai Rama Krishna Malladi<sup>1</sup>✉

Liquid cell transmission electron microscopy (LCTEM) is a powerful technique for investigating crystallisation dynamics with nanometre spatial resolution. However, probing phenomena occurring in liquids while mixing two precursor solutions has proven extremely challenging, requiring sophisticated liquid cell designs. Here, we demonstrate that introducing and withdrawing solvents in sequence makes it possible to maintain optimal imaging conditions while mixing liquids in a commercial liquid cell. We succeeded in visualising a fast nanoscale crystallisation mechanism when an organic molecule of R-BINOL-CN dissolved in chloroform interacts with methanol. The scanning transmission electron microscopy images recorded in real-time during the interaction of the two volatile solvents reveal the formation of chain-like structures of R-BINOL-CN particles, whereas they coalesce to form single large particles when methanol is absent. Our approach of mixing liquids establishes a platform for novel LCTEM studies of a wide range of electron-beam-sensitive materials, including drug molecules, polymers and molecular amphiphiles.

Liquid cell transmission electron microscopy (LCTEM) has evolved significantly over the past decade to become an unrivalled technique for investigating material growth processes in liquids in real-time and with atomic spatial resolution<sup>1–6</sup>. The most common way to image a liquid inside a transmission electron microscope (TEM) is by encapsulating a small volume of liquid between two electron-transparent layers, usually made of graphene or silicon nitride, to form a liquid cell (LC)<sup>7,8</sup>. Commercially available liquid cell holders employ chips with amorphous silicon nitride windows that contain one liquid. In order to perform experiments involving two or more reagents, a holder where liquid mixing happens shortly before reaching the LC has been previously utilised to investigate the crystallisation of calcium carbonate<sup>9</sup>. Since the liquids are pre-mixed just before entering the viewing area for imaging in the microscope, this approach restricts the ability to visualise important reactions that occur during the instance at which the solutions mix. Furthermore, the exact manner of flow of the two

liquid streams and the position and extent of reagent mixing were reported to be unclear in this study.

Due to the shortcomings of the above-mentioned technique, a specialised 2D heterostructure mixing cell was developed to visualise the same calcium carbonate synthesis, allowing for the controlled mixing of precursors in the vicinity of the electron beam<sup>10</sup>. However, the applicability of this method is restricted to the study of particles or clusters that are a few tens of nm in size and formed during the early stages of a solution-phase reaction. Additionally, the electron dose needed to crack the MoS<sub>2</sub> layer in order to initiate the mixing of the two solvents is very high, thereby making this design unsuitable for studying beam-sensitive specimens. Another study demonstrated solvent exchange in a commercial holder by following the self-assembly of an amphiphilic block copolymer into vesicular structures<sup>11</sup>. However, as the mixing process was complicated and not well controlled, the formation of vesicular structures failed often. Moreover, imaging was

<sup>1</sup>Department of Materials Science and Metallurgical Engineering, Indian Institute of Technology Hyderabad, Kandi, Sangareddy, Telangana, India. <sup>2</sup>Ernst Ruska-Centre for Microscopy and Spectroscopy with Electrons and Peter Grünberg Institute, Forschungszentrum Jülich GmbH, Jülich, Germany. <sup>3</sup>Advanced Organic Photonic Materials and Technology Laboratory, School of Chemistry and Centre for Nanotechnology, University of Hyderabad, Gachibowli, Hyderabad, India. <sup>4</sup>Institute of Energy and Climate Research, Fundamental Electrochemistry (IEK-9), Forschungszentrum Jülich GmbH, Jülich, Germany. <sup>5</sup>TESCAN Brno s.r.o., Brno, South Moravia, Czechia. <sup>6</sup>DENSsolutions B.V., Delft, The Netherlands. ✉e-mail: [r.dunin-borkowski@fz-juelich.de](mailto:r.dunin-borkowski@fz-juelich.de); [srkm@msme.iith.ac.in](mailto:srkm@msme.iith.ac.in)

performed in TEM rather than scanning TEM (STEM) mode, limiting the achievable contrast through the liquid layers and making it difficult to control the electron dose per pixel. In general, image contrast and radiation damage have limited the capabilities of LCTEM for studies of the dynamics of organic specimens<sup>12</sup>. In part for this reason, only a handful of LCTEM studies have reported the details of self-assembly processes in organic materials<sup>13–16</sup>. New strategies for minimising electron dose involve using direct electron detectors and imaging in STEM mode with reduced pixel dwell times and beam currents<sup>17</sup>.

Despite the several advances in LCTEM techniques for understanding nucleation and growth mechanisms, a reliable solvent mixing methodology is still lacking, making it highly challenging to visualise the dynamics of two-solvent phenomena in beam-sensitive specimens with sufficient spatial resolution. In this study, we present an LCTEM methodology that allows mixing two liquids and is capable of following the growth kinetics of beam-sensitive materials in STEM mode. In order to demonstrate the capability of our mixing technique, we elucidate a fast precipitation process, namely antisolvent crystallisation (ASC). ASC is a widely employed method in the pharmaceutical industry to produce ultrafine drug particles<sup>18</sup>. ASC uses two miscible solvents, one of which can dissolve the molecule of interest and one cannot (the so-called antisolvent). The antisolvent triggers rapid desolvation of molecules, resulting in instantaneous precipitation<sup>19</sup>. This method offers flexibility to control the amorphous or crystalline forms of active pharmaceutical ingredients (APIs) and helps to achieve high drug loadings<sup>20</sup>. Apart from a previous unsuccessful attempt to induce crystallisation through the antisolvent method<sup>21</sup>, to the best of our knowledge, no real-time observations of the ASC process have been reported using *in situ* liquid cell electron microscopy. Here, we demonstrate the ASC process of a beam-sensitive organic molecule (R-BINOL-CN) involving mixing two different volatile solvents using a commercially available LC.

## Results and discussion

### Material and Ex situ characterisation

Chirality is an important concept for the development of drugs and progress in the pharmaceutical industry<sup>22</sup>. A vital aspect of developing APIs is the determination of the enantiomeric purity of chiral therapeutic agents<sup>23</sup>. In drug discovery, R-BINOL has been used as a nuclear magnetic resonance solvating agent to distinguish between enantiomers of antitumor alkaloids<sup>24</sup> and natural isoflavanones<sup>25</sup>. In order to study ASC, we utilised the push-pull-type chiral donor-acceptor (D-A) molecule (+)-4,4'-(2,2'-diethoxy-[1,1'-binaphthalene]-6,6'-diyl) dibenzonitrile (R-BINOL-CN) (See Fig. 1a, Supplementary Note 1 and Supplementary Figs. 1–6). The solvent is chloroform, while the anti-solvent is methanol. Adding methanol increases the supersaturation of R-BINOL-CN in the solution, leading to the nucleation and growth of crystals<sup>26</sup>. Ex situ TEM and field emission scanning electron microscopy (FESEM) studies have shown that when R-BINOL-CN is dissolved in chloroform, and methanol is added to the solution, spherical particles self-assemble into  $\mu\text{m}$ -sized assemblies. The particle size and morphology depend on the solution ageing time and the amount of methanol added. (Supplementary Figs. 7–11). For self-assembly, 2 mg of R-BINOL-CN was dissolved in 2 mL of  $\text{CHCl}_3$  in a clean vial, followed by layering the solution with 2 mL of MeOH (Fig. 1a). The solution was kept undisturbed at room temperature for ASC. The self-assembly of R-BINOL-CN from the mother liquor was performed on different days to monitor the ASC products using optical microscopy, ex situ TEM and FESEM. Drop-casting the mother liquor (20  $\mu\text{L}$ ) onto a clean glass coverslip after a day of solution preparation produced discrete microspheres of various diameters ranging from  $\sim 1$  to 6  $\mu\text{m}$  (Fig. 1b). Performing the same experiment after two days revealed the formation of micropods due to the fusion of most of the microspheres into dimers, trimers, tetramers, pentamers, etc. (Fig. 1c). After three days, the self-assembly produced clear acicular microrods, indicating the transformation of micropods gradually into microrods. Further, the reduction in the width of the microrods signifies the stretching of the micropods along their long axis (Fig. 1d, h).

Preliminary ex situ TEM studies were also performed to estimate the size and morphology of particles formed via the ASC process. These experiments were done on copper grids with continuous carbon support film (Agar Scientific). The solution was prepared by dissolving 1 mg of R-BINOL-CN in 1 mL of chloroform, to which 0.6 mL of methanol was added. This solution (20  $\mu\text{L}$ ) was immediately dropped onto the TEM grid and allowed to dry for a few minutes before loading it in the TEM holder. The experiments were performed on a JEOL 2100 microscope, with a LaB<sub>6</sub> emitter operating at 200 kV. We observed that most particles existed as individual spheres (Fig. 1e, f and Supplementary Fig. 11). However, we identified a few particles which had already formed dimers and micropods (Fig. 1e and f). The mean particle radius was measured to be approximately 265 nm. Selected area diffraction patterns obtained at low dose confirm that the particles were crystalline (Fig. 1g and Supplementary Fig. 12).

### Liquid mixing in LCTEM

Most commercial LC holders are based on the bathtub design<sup>13,27–34</sup>. Here, the holder tip is designed such that liquid accumulates within a tiny well<sup>32,33</sup> containing two silicon chips with electron-transparent SiN membranes facing each other, thereby creating a narrow gap through which liquid flows due to capillary action. An interchangeable PEEK tubing transports the liquid from the syringe pump to the tip of the holder in the microscope column. To perform our experiments, we used the DENSolutions Ocean holder consisting of two Si chips with SiN windows of thickness  $\sim 50$  nm and dimensions  $\sim 25 \mu\text{m} \times 400 \mu\text{m}$ . There are a few studies where liquid mixing experiments were performed using this holder. Therefore, we first tried to investigate the possibility of using such holders to follow the antisolvent precipitation process involving the mixing of two volatile solvents. One of the previous studies on mixing liquids using the DENSolutions Ocean holder used a straightforward drop-casting technique<sup>13</sup>. Here, the first solution was drop cast on the silicon nitride window of the bottom chip. Then, the top chip was placed above the droplet, and the cell was assembled. The second liquid was then flowed into the holder using a syringe pump. However, this way of mixing could not be adopted for our experiments due to the highly volatile nature of the solvents. During our ex situ TEM studies and preliminary *in situ* TEM studies using the Ocean holder, we noticed that a tiny droplet of R-BINOL-CN dissolved in chloroform evaporated in less than 10 s, and it was impossible to assemble the chips and align the windows within this timeframe. Therefore, this method was unsuitable for experiments involving volatile solvents.

The other study used air to push the excess solution left within the area of the bathtub<sup>11</sup>. Once the bathtub area was emptied, the second solution was introduced into the holder. This method might be successful for aqueous solutions, but in our case, due to the highly volatile nature of chloroform, using air to push the excess liquid resulted in the evaporation of chloroform that was initially present between the chips. Furthermore, due to the very high flow resistance and the possibility of liquid flow not being confined to a specific path in the bathtub design, liquid mixing may occur outside the viewing area itself. Since anti-solvent precipitation occurs instantaneously, it is pivotal that methanol interacts with the chloroform only inside the viewing area to be able to have any chance of capturing this process. We attempted to introduce methanol using this approach but were unsuccessful in visualising the process. Thus, the Ocean holder based on the bathtub design was deemed unsuitable for carrying out anti-solvent precipitation. It was also observed that controlling the liquid thickness was difficult using this holder even while imaging a single liquid (Supplementary Movies 13 and 14). Instead, we chose to use the DENSolutions Stream holder (Supplementary Movies 8–12) in which the liquid flow path is confined to a defined channel, where the control over liquid thickness is significantly better due to the ability to push and pull liquids in and out of the viewing area. Initial trials performed using this holder showed improved image contrast (Supplementary Movie 15). Additionally, theoretical studies strongly support the applicability of holders with on-chip inlets and outlets for achieving mixing within the viewing area of the liquid cell<sup>35</sup>.

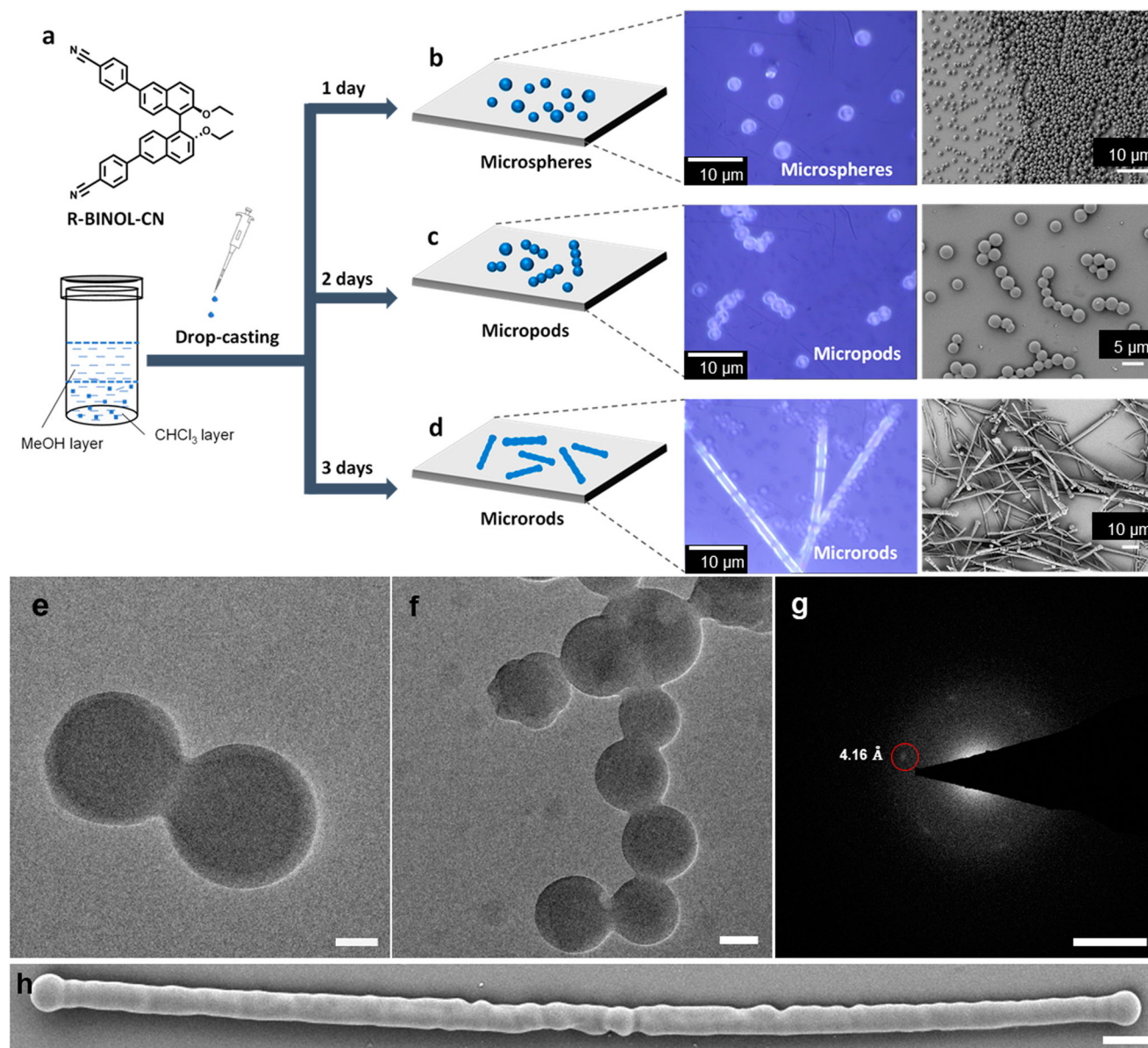


**Fig. 1 | Overview of the ex situ self-assembly process.** **a** Molecular structure of R-BINOL-CN. **b–d** Schematic representation and optical and FESEM images of R-BINOL-CN microspheres, micropods, and microrods obtained via self-assembly from CHCl<sub>3</sub>/MeOH solution (1:1) ratio at different ageing. **e, f** Bright field (BF)-TEM images showing particles formed by drop-casting a solution of ratio 1: 0.6, R-BINOL-CN in chloroform to methanol, on a carbon grid. Two particles forming a

neck and multiple particles are necked together forming a micropod. Scale bars are (e) 100 nm (f) 200 nm (g) Selected area diffraction pattern (SADP) obtained at low-dose (0.1 e<sup>-</sup>/Å<sup>2</sup>) from the near-spherical particles similar to those shown in (e, f). Scale bar for the diffraction pattern is 2 nm<sup>-1</sup>. **h** FESEM image of R-BINOL-CN drop cast on glass coverslips after ageing the solution for 4 days. Scale bar is 2 μm.

There are other commercially available holders from Hummingbird Scientific consisting of dual inlets, offering the possibility to perform solvent mixing experiments. A few studies where reactions occurring while mixing two different solvents have been investigated using such liquid flow TEM holders<sup>9,36</sup>. These systems have two inlets that terminate within a few centimetres of the liquid cell, facilitating the liquid streams to mix and flow through and around the viewing area of the liquid cell. The availability of two inlet channels is beneficial for flowing each liquid separately with desired flow rates, thereby providing better control over the ratio of reagents that are being mixed and also ensuring that a constant overall flow rate can be maintained. Recently, Merckens et al. proposed the concept of a diffusion cell that relies on diffusive mass transport near the viewing area, significantly improving important characteristics of LP-TEM flow reactors, particularly offering rapid solution exchange dynamics<sup>35</sup>. In addition to such new designs, Insight chips have

developed liquid cells containing multiple channels that open possibilities for mixing liquids inside the viewing area<sup>37</sup>.

The in situ LC-TEM observations were carried out in a JEOL JEM F-200 Multipurpose TEM equipped with a cold field emitter and using a liquid flow holder (Stream) and LC (Nano-Cell, DENSSolutions). The Nano-Cell comprises two micro-electromechanical systems (MEMS) based chips sandwiched to form a sealed chamber<sup>38</sup>. Both chips have rectangular electron-transparent 50-nm-thick silicon nitride windows. (Supplementary Fig. 15). Using the tool provided with the holder, the two windows can be aligned to provide a viewing area through which imaging can be carried out. (Supplementary Fig. 16). The Nano-Cell is mounted into a dedicated holder capable of connecting the cell assembly to a syringe or pressure-based pump. The lower MEMS chip has an on-chip inlet and outlet, as well as spacers that create a well-defined microfluidic channel, facilitating a regulated flow of liquid across the viewing area of the cell. (See Supplementary Note 2).

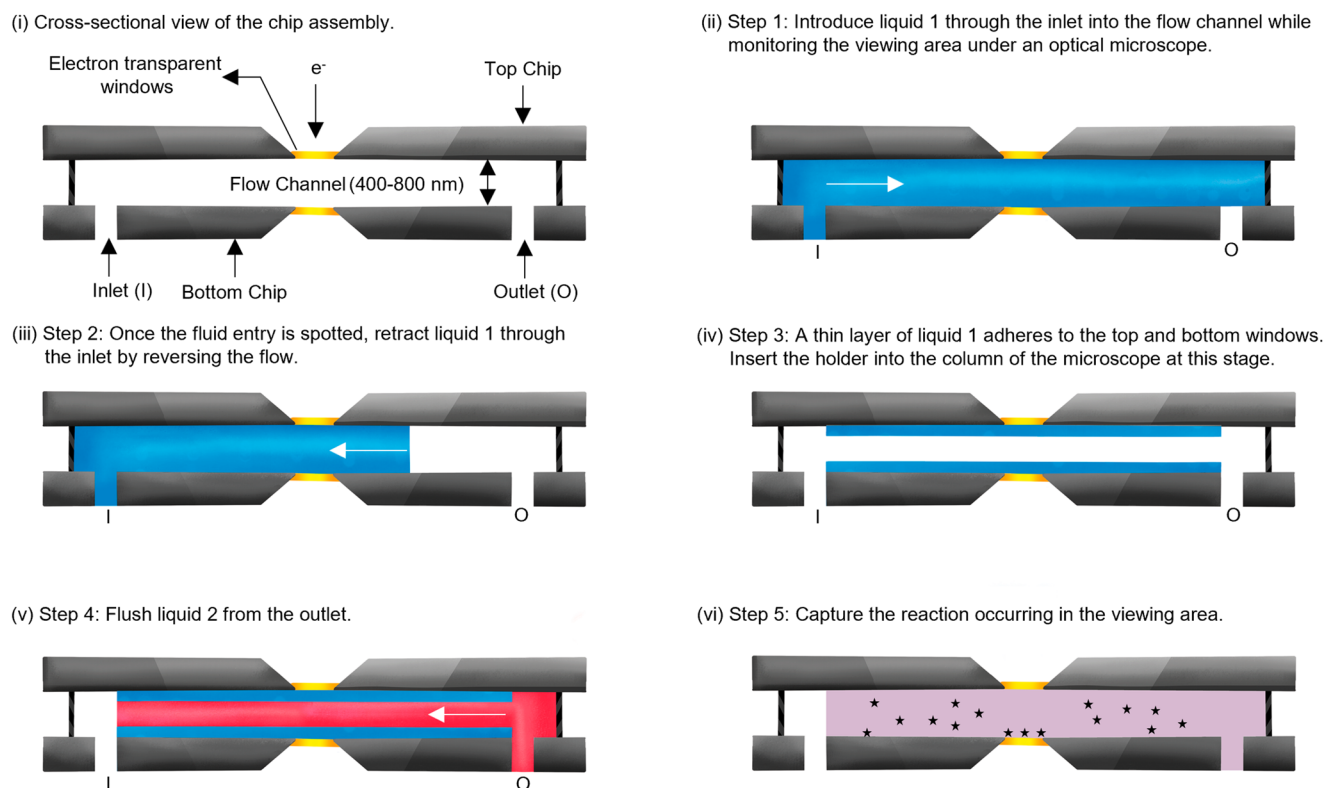


**Fig. 2 | Schematic diagrams of the liquid mixing procedure.** **i** Cross-sectional view of the Nano-Cell assembly, consisting of a top chip and a bottom chip, as well as an inlet and outlet on the bottom chip. The on-chip microfluidic flow channel defined by the spacers ensures controlled flow from the inlet to the outlet. Both chips have electron-transparent windows to facilitate imaging. **ii–vi** Steps involved in mixing R-

BINOL-CN dissolved in chloroform (liquid 1 - blue) and methanol (liquid 2 - red), leading to antisolvent crystallisation. Black stars in **(vi)** represent R-BINOL-CN particles, which precipitate spontaneously during the ASC process. White arrows in **(ii)**, **(iii)**, and **(v)** denote the direction of liquid flow.

Our strategy to mix two volatile organic solvents in the viewing area of the microscope is as follows (See Supplementary Movie 1). Once the Nano-Cell is aligned and assembled in the holder (Fig. 2-i), a 1.8 mM solution of R-BINOL-CN dissolved in chloroform is introduced into the cell at the slowest flow rate of the syringe pump, which is connected to the inlet valve of the holder (Full control of the flow rate is not possible due to the high flow resistance). The viewing area is monitored continuously under an optical microscope to identify liquid entry into the cell. Once the liquid fills the viewing area (Fig. 2-ii), the direction of flow is reversed, such that the liquid front is pulled backwards (Fig. 2-iii), leaving some liquid adhering to the windows (Fig. 2-iv). At this stage, the holder is inserted into the microscope. Now, using a syringe pump connected to the outlet valve of the holder, methanol is introduced at a rate of 2  $\mu\text{L}/\text{min}$  into the Nano-Cell (Fig. 2-v). The flow is stopped once it enters the viewing area in order to maintain a liquid thickness that is as low as possible and achieve the best possible contrast. While LC experiments are often performed in TEM mode with poor image contrast, the use of STEM mode proves beneficial for imaging thicker specimens<sup>39</sup> and organic materials<sup>40,41</sup>. Therefore, here, ADF-STEM mode (camera length = 200 mm) is used to record the dynamics of particle formation and growth, the microscope is operated at 200 kV, and the electron dose is optimised by using a combination of spot size and aperture. (See Supplementary Note 3). The electron dose ( $e^-/\text{\AA}^2$ ) was calculated using the electron beam current, pixel dwell time and pixel size<sup>42</sup>. We calculated the dose per frame by dividing the probe current at the sample,  $i_e$  (C/s), by the scan area  $A$  ( $\text{\AA}^2$ ) and multiplying by the frame time ( $t_f$ ) as follows: ( $i_e \cdot t_f$ ) /  $e \cdot A$  ( $e$  is the elementary charge, C/electron and  $t_f = 2.16$  s).

### LC-TEM of antisolvent crystallisation

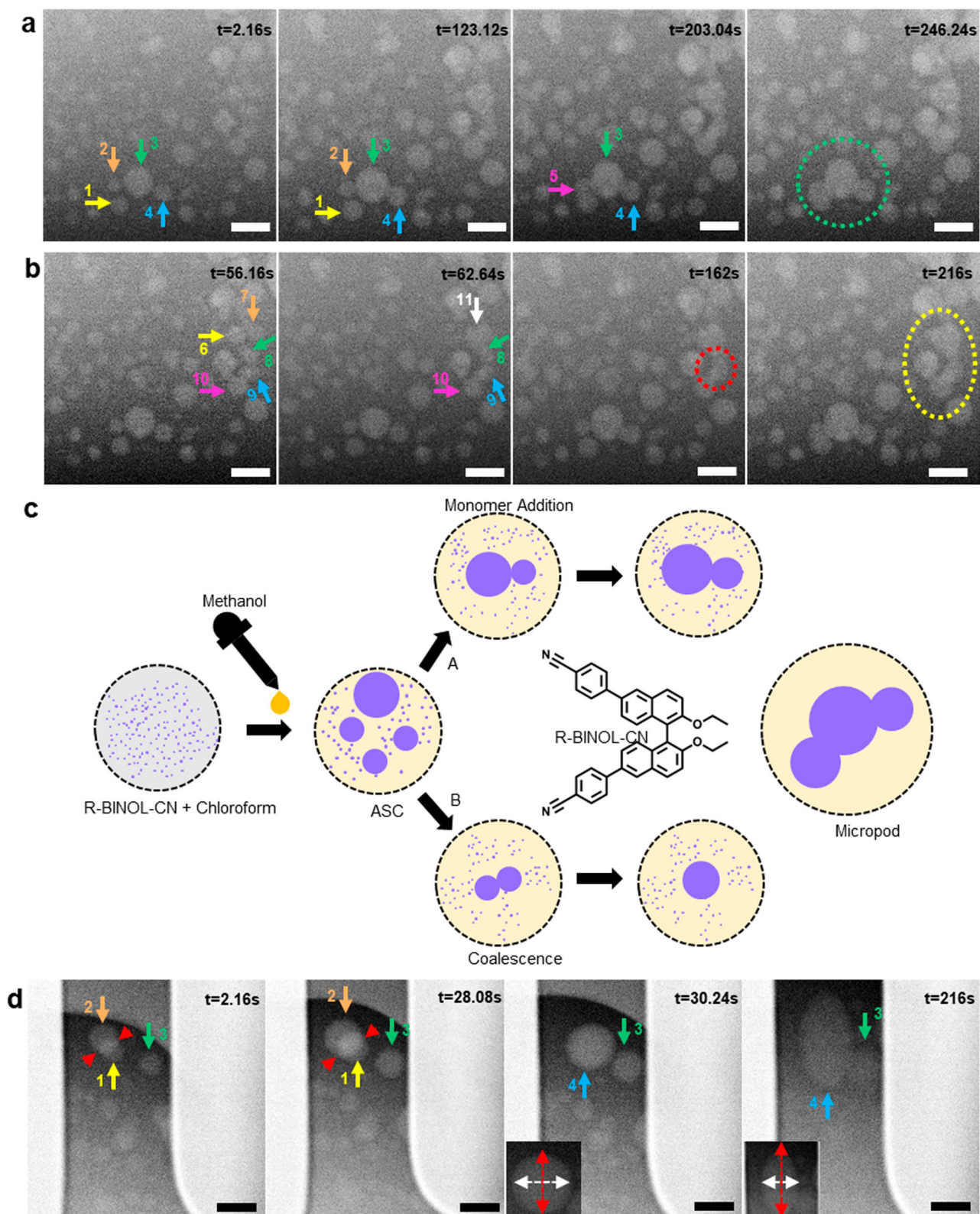
Snapshots (Fig. 3) from a time series (Supplementary Movie 2) show the evolution of the precipitation process as methanol interacts with R-BINOL-

CN in chloroform in the Nano-Cell. As soon as methanol enters the viewing area (Fig. 3a,  $t = 2.16$  s), nucleation and growth occur instantaneously, with many R-BINOL-CN particles with spherical morphology appearing across the field of view. To the best of our knowledge, this is the first time antisolvent precipitation has been visualised in real-time.

The growth of four particles, which are labelled 1 to 4 and have initial radii of  $\sim 215$ ,  $\sim 155$ ,  $\sim 385$  and  $\sim 230$  nm, respectively, is followed in Fig. 3a. All four particles initially grow via monomer attachment ( $2.16 < t < 123.12$  s). At  $t = 123.12$  s, the surfaces of particles 2 (195 nm) and 4 (270 nm) touch that of particle 3 (450 nm). Nevertheless, no coalescence occurs, and the growth process continues *via* monomer addition. In contrast, when the radii of particles 1 and 2 grow to 270 and 215 nm, respectively, their surfaces touch, leading to coalescence and forming a larger particle 5 with a radius of  $\sim 360$  nm ( $t = 203.04$  s).

Subsequently ( $203.04 < t < 246.24$  s), despite the surfaces of particles 3, 4, and 5 being in contact, no further coalescence takes place and the three particles ‘neck’ together, forming a so-called micropod ( $t = 246.24$  s) (Fig. 3c). A similar growth trend is observed in another cluster comprising five particles (Fig. 3b). Particles 6 and 7 (radius  $\sim 230$  nm) coalesce to form a larger particle 11 (radius  $\sim 320$  nm), whereas particles 9 (radius  $\sim 250$  nm) and 10 (radius  $\sim 280$  nm) neck to each other. Particles 8, 9 and 11 also form a neck as they touch each other ( $t = 162$  s, red dotted region), ultimately creating a new micropod ( $t = 216$  s). Based on the two groups of particles analysed, the growth of individual particles by either monomer attachment or coalescence is influenced by the dimensions of other nearby particles, such that a resulting micropod consists of nearly uniformly sized particles. This result is consistent with *ex situ* TEM data (Supplementary Fig. 11), which indicates that micropods consist of similarly sized particles.

From Fig. 3a ( $t = 123.12$  s), we observe that particle 3 does not fuse with particles 2 and 4 when they touch each other. Since there are two silicon



nitride windows, one on top and one on the bottom, it is essential to confirm whether adjacent particles coalesce into a large solid object or visually overlap in the projection. In order to establish that particles 2, 3 and 4 are growing on the same membrane and to support our coalescence claim, we performed an ex situ structural characterisation on the bottom chip at the end of the in situ experiment. Although the same particles aggregated during

the in situ experiment had delaminated from the window surface, similar aggregates were formed outside the viewing area (Supplementary Movie 3).

To provide further evidence, we repeated the mixing experiments to capture coalescence events between particles growing on different silicon nitride windows (Supplementary Movie 4). The growth of three particles labelled 1 to 3 and having initial radii of  $\sim 290$ ,  $\sim 350$ , and  $\sim 275$  nm,

**Fig. 3 | Anti-solvent crystallisation process and mechanisms of particle formation.** **a** Snapshots from an in situ ADF-STEM movie of the ASC process (Dose rate:  $0.01 \text{ e}/\text{\AA}^2 \cdot \text{s}$ ; Total dose:  $1.18 \text{ e}/\text{\AA}^2$ ). The growth of four particles labelled 1–4 (yellow, orange, green and blue arrows, respectively) can be observed from the time-resolved STEM images. The green dotted region marks a micropod. **b** Snapshots from the same movie following the growth of five particles labelled 6–10 (yellow, orange, green, blue and pink arrows, respectively). The red dotted region marks the necks formed between particles 8, 9 and 11. The yellow dotted region represents a micropod. All scale bars are  $1 \mu\text{m}$ . **c** Schematic diagram showing the mechanism of

micropod formation during the ASC process. A solution containing monomers of R-BINOL-CN (violet dots) dissolved in chloroform (grey) upon methanol (yellow drop) addition results in the instantaneous precipitation of particles (violet discs). Pathway (A): growth by monomer addition; Pathway (B): growth *via* coalescence. **d** Snapshots from an in situ ADF-STEM Movie showing the growth of R-BINOL-CN particles labelled 1–3 *via* anti-solvent crystallisation because of methanol addition (Dose rate:  $0.01 \text{ e}/\text{\AA}^2 \cdot \text{s}$ ; Total dose:  $1 \text{ e}/\text{\AA}^2$ ). At  $t = 2.16 \text{ s}$  and  $t = 28.08 \text{ s}$ , the red arrows indicate a brighter region, wherein particles growing on the top and bottom windows overlap before coalescing. All scale bars are  $1 \mu\text{m}$ .

respectively, is followed in Fig. 3d. It can be seen that particles 1 and 2 are growing on different windows from the bright contrast (thickness contrast) obtained from the overlapping region (red arrows in  $t = 2.16 \text{ s}$ ). All the particles grow *via* monomer attachment, similar to what was observed in Fig. 3a. At  $t = 28.08 \text{ s}$ , the overlapping region between the particles increases as the size of the individual particle increases (red arrows in  $t = 28.08$ ). The edges of both particles are clearly distinguishable. In this instance, particles 1 and 2 come in contact and coalesce to form the larger particle 4, which grows with time. However, particle 4 did not coalesce with the adjacent particle 3 but started elongating in one direction. We calculated the dimensions of particle 4 during this period ( $30.4 < t < 216 \text{ s}$ ). The aspect ratio (length to width) of this particle changed from 0.97 (nearly circular) to 0.55 (elongated). This kind of growth was seen only in rare cases.

Statistical analysis of multiple videos of precipitation events (Supplementary Movie 2) allows for a detailed understanding of the mechanism of particle growth. We used a Python script to identify and track particles in each frame of one movie (Fig. 4a). (See Supplementary Note 5). At the start, 56 particles are in the field of view. (Supplementary Fig. 24). This number first increases slightly (Fig. 4b;  $0 < t < 10 \text{ s}$ ) as particles that nucleated during the mixing process but which were too small to be identified grow as they interact with methanol. The number of particles remains constant ( $10 < t < 246.24 \text{ s}$ ).

Next, we study the growth of 5 particles that cover the entire viewing area (Fig. 4c). We find a slow growth rate of  $\sim 0.1 \text{ nm/s}$  for particles with initial radii of 100–300 nm and a higher growth rate of  $0.52 \text{ nm/s}$  for a particle of radius 700 nm. A comparison between the initial and final particle distribution (Fig. 4d) shows that the particle radii mostly remain in the range of 100–300 nm, with the mean particle radius increasing from 202 nm ( $\pm 5 \text{ nm}$ ) to 210 nm ( $\pm 3 \text{ nm}$ ). The larger size of particle 14 (Fig. 4a) may reflect the sensitivity of the ASC process to local liquid mixing, as poor antisolvent mixing can create regions with high local supersaturation, resulting in excess primary nucleation and leading to fine particle formation and agglomeration<sup>43</sup>. Another probable reason for such higher growth rates is Ostwald ripening. The inability to acquire compositional information inside such microfluidic channels during the experiment makes it difficult to quantify the degree of supersaturation. Hence, the process is confirmed as antisolvent crystallisation by relying mainly on visual evidence, which is the formation of particles as observed in our in situ and ex situ studies. Similar observations on controlling the shape and size of lead halide perovskite nanocrystals *via* antisolvent crystallisation have been recently reported.

The critical factor for producing ultrafine particles *via* antisolvent precipitation is maintaining conditions that result in rapid particle formation, with limited or no particle growth<sup>19</sup>. Thus, during the ASC process, a nearly constant number of particles with time, slow growth rates and similar initial and final particle size distributions are expected. Our statistical analysis confirms the same, thereby illustrating the suitability of our methodology for fully characterising the most relevant aspects of ASC. All these observations also highlight the suitability of the LCTEM methodology for optimising API production *via* an ASC route.

### Growth kinetics in the absence of the antisolvent

In order to confirm the role of the antisolvent, we studied the growth kinetics of R-BINOL-CN dissolved in chloroform in the absence of methanol. We introduced an R-BINOL-CN solution with a similar concentration of 1.8 mM into the Nano-Cell by following the same procedure (up to the

introduction of the methanol) (Fig. 1ii–iv). This time, the energy of the electron beam was used to nucleate R-BINOL-CN particles by parking the beam at a specific location for 2–3 s. (See Supplementary Note 4).

Figure 5 and Supplementary Movie 5 show the growth kinetics of two R-BINOL-CN particles that nucleated ( $t = 2.16 \text{ s}$ ) and started growing *via* monomer attachment ( $t = 49.68 \text{ s}$ ). Here, we observe the influence of the narrow channels on the shape of the particles. For large particles (radius  $> 1 \mu\text{m}$ ), the shape changed from spherical to disc like morphology. The disc like particles touch and coalesce to form a single larger particle ( $t = 54 \text{ s}$ ). This particle then keeps growing until it fills the entire viewing area of the Nano-Cell ( $t = 168.48 \text{ s}$ ). Before coalescing, the growth rate of both particles (Fig. 5c) follows a linear trend, with the larger particle growing at approximately  $22 \text{ nm/s}$ , compared to the smaller particle which grew at  $8.5 \text{ nm/s}$ . The coalescence of the two particles, which contrasts with the formation of a micropod in the presence of methanol, highlights the crucial role of the antisolvent. We repeated this nucleation method and followed the growth of a few more particles (Fig. 5b,  $t = 2.16 \text{ s}$ ) (See Supplementary Movie 6). Here, we find that particle growth proceeds *via* monomer attachment and Ostwald ripening (OR)<sup>44</sup> is also observed. It is seen that within this field of view, particle 3 grew with time, whereas particle 4 kept shrinking as monomers diffused across, assisting the growth of the larger particle ( $2.16 < t < 470.84 \text{ s}$ ). Figure 5d shows the growth and dissolution rates of particles 3 and 4, with the smaller particle dissolving at  $0.7 \text{ nm/s}$ .

### Visualising particle attachment at the nanoscale

The ex situ images (Supplementary Figs. 7 and 11) reveal the formation of long chain-like structures of identically-sized attached particles. We investigated whether this type of self-assembly could be due to the oriented attachment (OA) of mutually oriented particles within the solution<sup>45</sup>. In order to probe this phenomenon, we added a small fraction (0.1:1) of methanol to the solution containing R-BINOL-CN in chloroform ex situ and introduced it into the microscope. (Supplementary Movie 1).

In this study, we did not reverse the liquid flow in order to retain a sufficient liquid thickness to allow the particles to move instead of adhering to the surfaces of the windows. Here, we do not observe spatial confinement effects and the particles move freely, whereas there is always an influence of the membranes onto which the particles can adhere to in case of the mixing experiment. Figure 6 shows snapshots of the growth process from a time series (Supplementary Movie 7). Three particles of approximately 20 nm are initially present in the solution ( $t = 2.16 \text{ s}$ ). They move within the solution, encountering each other several times ( $2.16 < t < 123.12 \text{ s}$ ). For example, particles 2 and 3 meet each other at  $t = 103.68 \text{ s}$  but do not coalesce. Instead, they rearrange themselves ( $103.68 < t < 162 \text{ s}$ ) before undergoing attachment. Finally, particle 1 also attaches to particles 2 and 3 ( $t = 233.28 \text{ s}$ ). The attachment process observed here proceeds in several stages. First, two particles approach each other and make contact. They do not attach, but with time, one of the particles flips before undergoing attachment (Fig. 6g).

In order to gain insights into the crystallinity of these organic nanoparticles, we performed ex situ low-dose diffraction studies using a TESCAN TENSOR analytical 4D-STEM to study dry specimens that were drop-cast onto a C grid (Fig. 5h, i). Lattice spacings measured from the diffraction patterns (Fig. 6j–l) are in agreement with powder XRD data (Supplementary Fig. 6 and Supplementary Table 1) and low-dose selected area diffraction (Supplementary Fig. 12) from R-BINOL-CN. From the 4D-STEM dataset, we observe crystallinity at several locations along the edges of the particles,

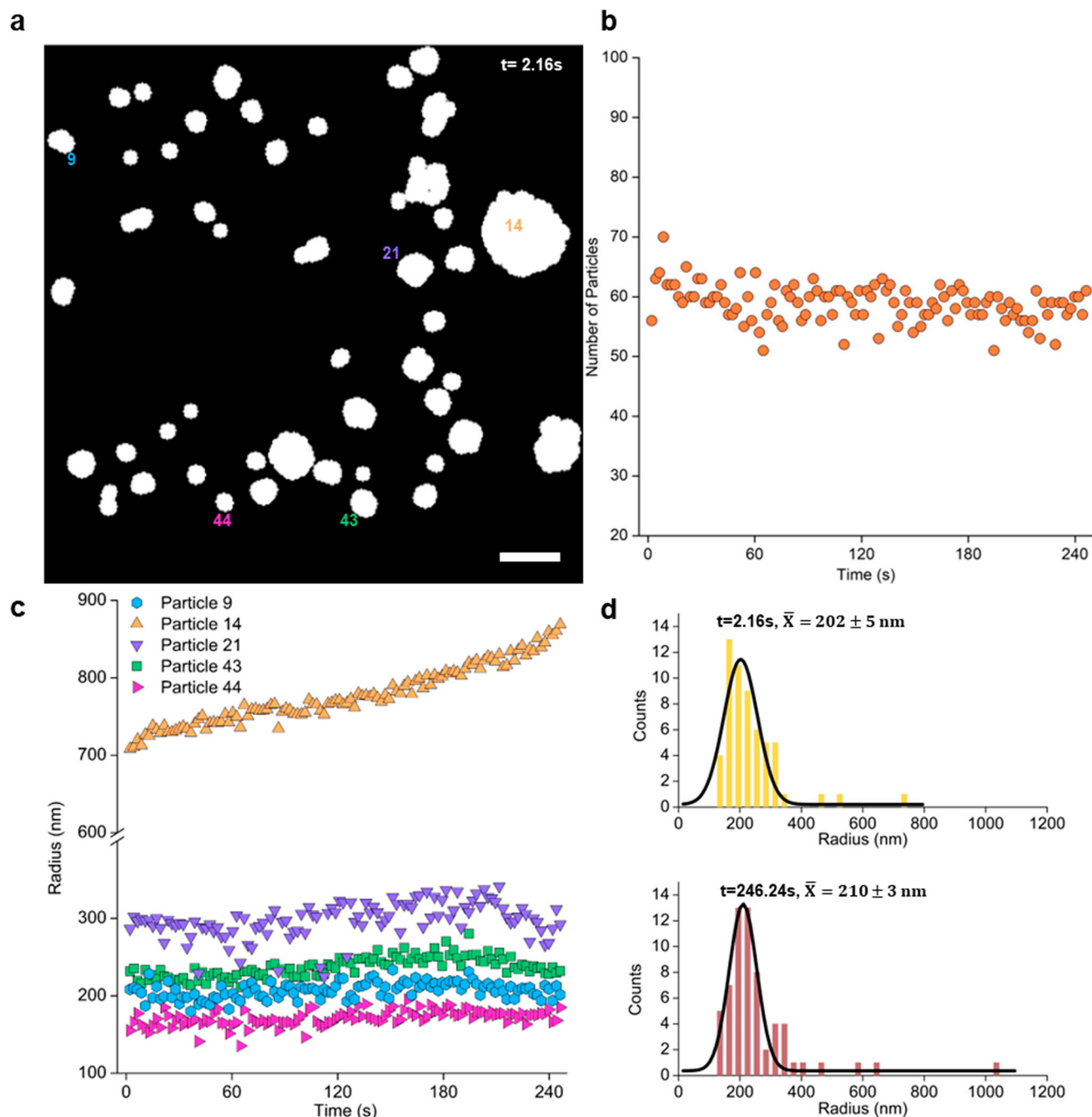


**Fig. 4 | Statistical analysis of the ADF-STEM movie of anti-solvent crystallisation.** **a** Thresholded image (multi-Otsu) of the first frame of the ADF-STEM movie of ASC. The growth rates of particles 9, 14, 21, 43 and 44 are followed. Scale bar is 500 nm. **b** The number of particles formed with time is calculated from the ADF-

STEM movie of ASC. **c** Plot illustrating the growth rates of the particles labelled in (a). **(d)** Histograms of initial (yellow bars) and final (brown bars) particle size distributions determined from the ADF-STEM movie of ASC. Black curves are Gaussian fits.

which are free from carbon support. (Supplementary Figs. 13 and 14). The results from our ex situ ageing experiments and diffraction studies, coupled with our LC-TEM observations and previous reports in the literature on the self-assembly of nanostructures during solution ageing<sup>46–49</sup>, suggest that OA along specific crystallographic planes might possibly be the reason for self-organisation. However, further detailed real-time 4D-STEM investigations are required to establish this observation as an oriented attachment process.

## Conclusions

In this study, we have developed a method for sequentially introducing two solvents into a commercially available liquid cell in a TEM, providing direct access to the visualisation of antisolvent crystallisation of an electron-beam-

sensitive chiral organic molecule in real-time. Our LC-TEM methodology offers new opportunities for the real-time imaging of reactions in a wide range of processes that involve reagent mixing, including self-assembly processes in liquid crystals, block copolymers, hydrogen-bonded and  $\pi$ -bonded complexes, as well as many natural polymers that are essential for developing new structures and devices across scientific disciplines<sup>50</sup>. In particular, block copolymer micelles, which are critical for drug delivery purposes<sup>51</sup>, can be formed via two solvent mixing reactions. Recently, crystallisation has been employed to control the self-assembly of polymeric and molecular amphiphiles in solution to fabricate non-spherical nanoparticles and sophisticated hierarchical assemblies<sup>52</sup>. Our LC-TEM technique provides a platform for obtaining a fundamental understanding of such

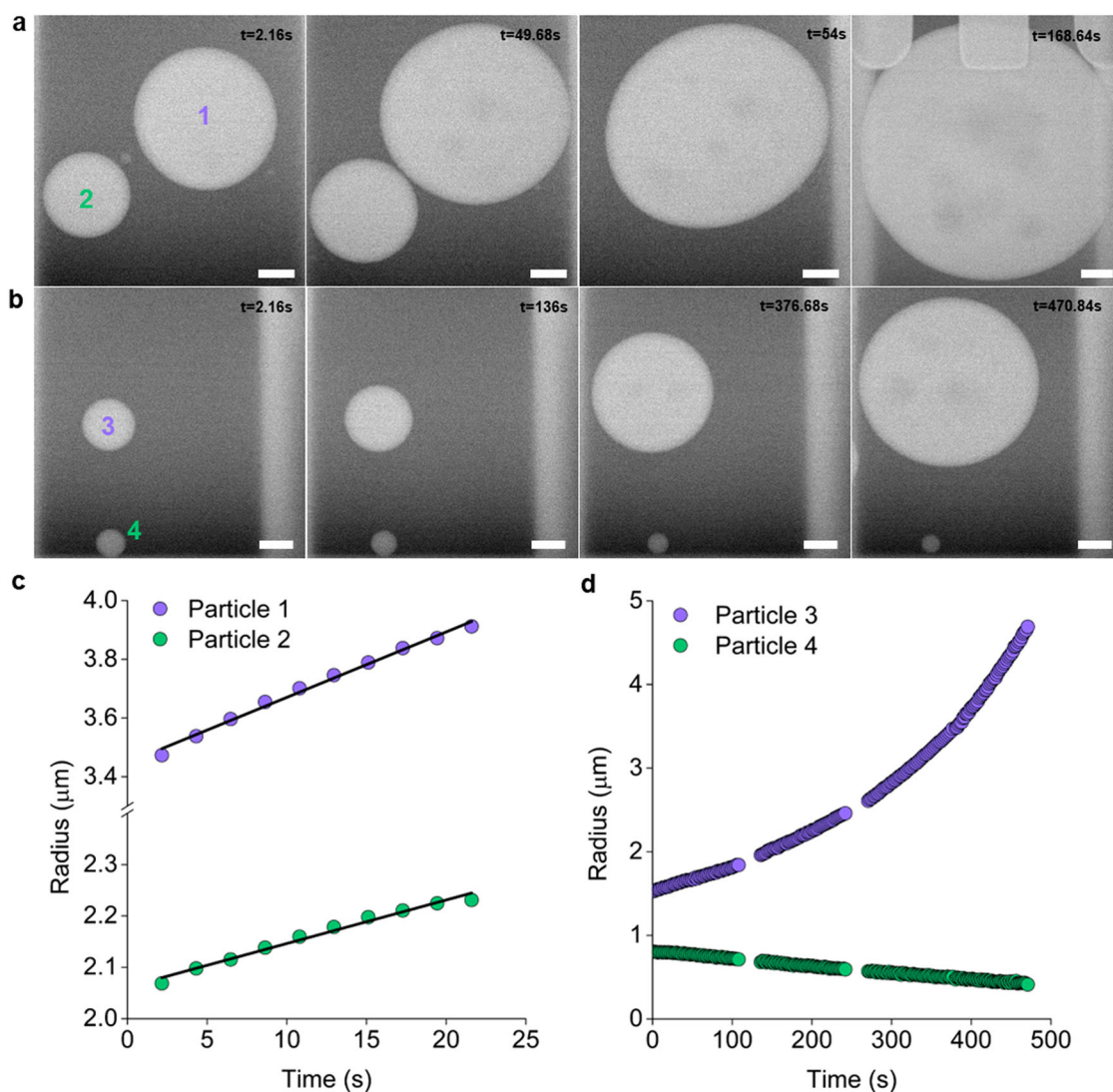


**Fig. 5 | Growth kinetics of R-BINOL-CN in the absence of methanol.** **a** Snapshots from an in situ STEM movie showing the growth of R-BINOL-CN particles nucleated using the electron beam. With time, particles 1 and 2 grow via monomer attachment, eventually coalescing to form a single larger particle. (Dose rate:  $0.03 \text{ e}/\text{\AA}^2 \cdot \text{s}$ ; Total dose:  $2.22 \text{ e}/\text{\AA}^2$ ). **b** Snapshots from an in situ ADF-STEM movie showing particle growth via Ostwald Ripening. Particle 3 keeps becoming larger, while particle 4 tends to dissolve. (Dose rate:  $0.02 \text{ e}/\text{\AA}^2 \cdot \text{s}$ ; Total dose:  $5.58 \text{ e}/\text{\AA}^2$ ). **c** Plot illustrating the growth rates of

particles 1 and 2 until they coalesce. A linear trend indicated a growth mediated by monomer attachment and controlled by the surface kinetics. The black line in the graph shows a linear fit to the data. **d** Plot showing growth and dissolution rates of particles 3 and 4. The gaps in the time axis are due to delays during long series capture in STEM mode. The timestamp has been adjusted in Fig. (b) (see Supplementary Note 4). All scale bars are  $2 \mu\text{m}$ .

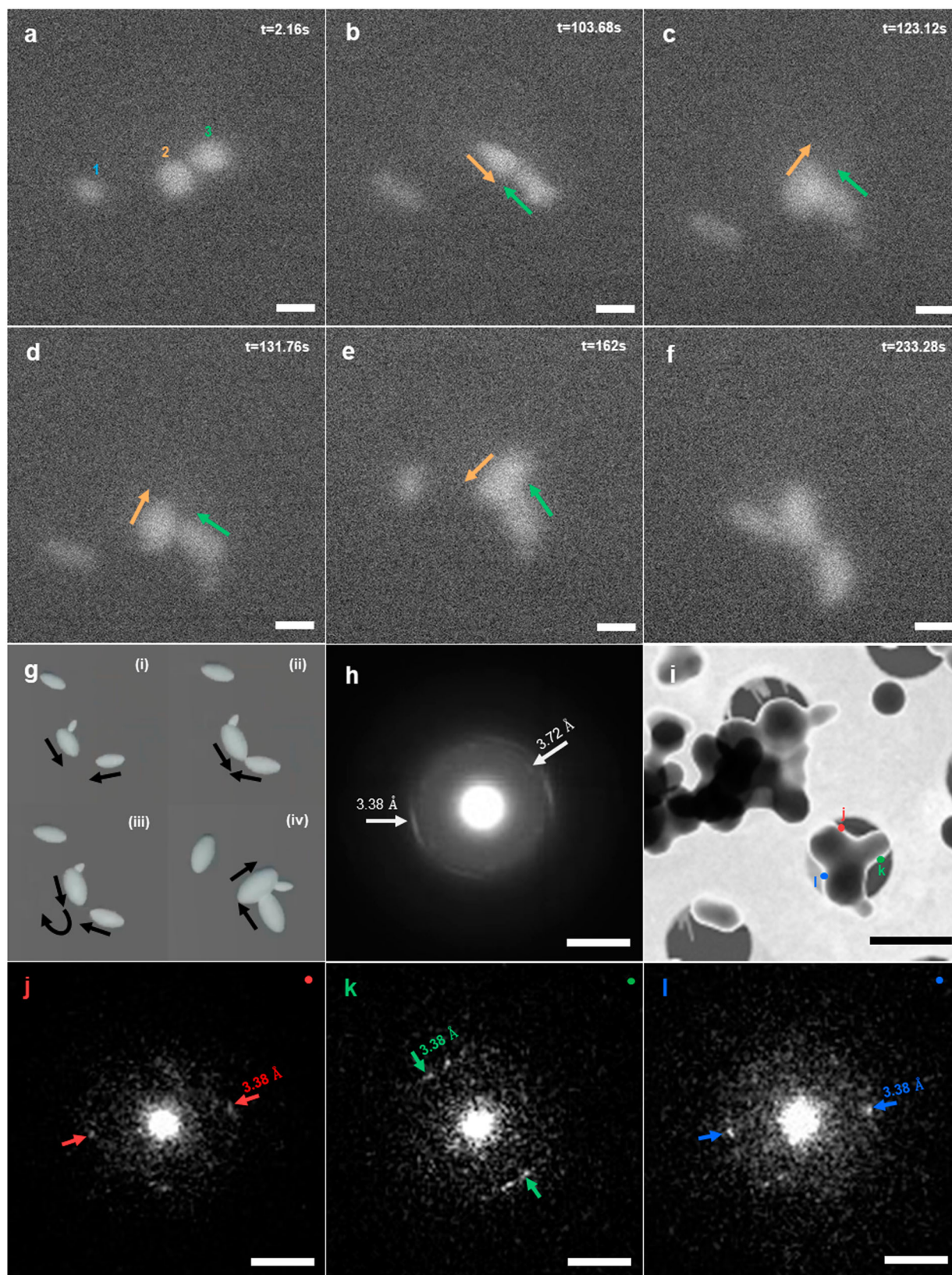
processes, which are essential for the reproducible synthesis of desired structures<sup>53</sup>.

Probing a spontaneous reaction such as ASC while mixing highly volatile solvents is essential for studying liquid mixing processes in a wide range of organic and inorganic solvents. The excellent signal-to-noise ratio of low-dose electron microscopy in STEM mode allows for the accurate quantitative analysis of the growth of electron-beam-sensitive organic crystals. In contrast to previous liquid mixing cells, our LC-TEM methodology allows for high-contrast imaging of the dynamics of particles ranging from the 10 nm to the 10  $\mu\text{m}$  scale. Using a combination of STEM mode for in situ imaging and low-dose 4D STEM techniques for ex situ studies provides excellent contrast and unparalleled insight into the crystallinity of extremely electron-beam-sensitive materials, which is not otherwise achievable when imaging in conventional TEM mode. Since in TEM mode, the dose control is not precise, as the beam is spread over a large area and the dose deposited on the specimen varies on the intensity as opposed to STEM mode where the dose per pixel can be fixed throughout the experiment<sup>42</sup>

Our study provides a route to the investigation of the self-assembly processes of soft materials, which can involve varying levels of complication, ranging from the simple dimerisation of two building blocks driven by hydrogen bonding to the formation of complex supramolecular architectures<sup>54</sup>. Our results not only strengthen the importance of LC-TEM as a platform for exploring complex chemical processes in real-time but also provide an impetus for developing on-chip flow channels to enable control over mixing rates directly in the viewing area in order to make it possible to perform experiments with greater precision<sup>55</sup>.

## Methods

In order to perform the liquid cell studies, a commercially available liquid flow holder (Stream) and liquid cell (Nano-Cell) from DENSSolutions B.V. was used. The Nano-cell design comprises two chips sandwiched to create a closed fluidic chamber. The lower chip contains a set of on-chip inlet and outlet, which is surrounded by a 200 nm SiNx spacer, creating a well-defined fluidic path. The top chip includes a dedicated groove to house an O-ring,



preventing the liquid from leaking into the TEM column. Both chips have an electron transparent window of  $20\text{ }\mu\text{m} \times 200\text{ }\mu\text{m}$  in dimension. The Nano-Cell is fully covered with silicon nitride, ensuring an inert environment for the liquid and the experiment. The side-entry holder that houses the Nano-Cell has a modular design which enables the possibility to remove the tip

where the Nano-Cell is assembled, such that one can easily replace the inner tube. This provision helps to prevent clogging and cross-contamination. During the experiments, this system provides the flexibility to choose the material of the tubing and the O-ring to provide the broadest possible chemical compatibility. The Nano-cell is assembled with the help of an

**Fig. 6 | Rearrangement and attachment of R-BINOL-CN particles with time observed by in situ STEM and ex situ 4D-STEM.** a–f Snapshots from an in situ ADF-STEM movie showing attachment of nanoparticles (Dose rate:  $28.53 \text{ e}/\text{\AA}^2 \text{ s}$ ; Total dose:  $6077.89 \text{ e}/\text{\AA}^2$ ). Three particles labelled 1–3 precipitated by ASC rearrange and attach to form a chain, as observed in time-resolved STEM images. Orange and green arrows in (b–e) mark the orientations of particles 2 and 3, respectively. The directions of the arrows change with time, showing how the particles rearrange before attaching. All scale bars in (a–f) are 20 nm. g Schematic diagram showing the steps in the attachment process. Black arrows indicate the orientations of the particles. h Integrated diffraction pattern obtained from low-dose 4D-STEM

measurements by summing 16384 diffraction patterns from each pixel in the Virtual Bright Field (VBF) STEM image shown in (i), scale bar here is 10 mrad. (i) VBF image obtained from a specimen of R-BINOL-CN dissolved in chloroform and methanol (in the ratio 1:0.8), drop-cast onto a Cu grid with a holey C supporting film. The scale bar is 500 nm. The diffraction patterns from the locations marked (j, k and l) in the VBF-STEM image (i), along the edges of the R-BINOL CN micropod, are shown in images (j), (k) and (l), respectively. Scale bar here is 10 mrad. The TIFF frame numbers corresponding to points (j, k and l) are 9551, 11103 and 11976, respectively, from the entire dataset.

alignment stage that is supplied along with the holder. This stage has an integrated optical camera and micrometre screws to align the top and bottom windows precisely.

To facilitate fluid flow, the back part of the holder has two manual valves at the sides. The inlet and outlet valves regulate the entry and exit of liquid into the holder. We connected a syringe pump (HOLMARC, HO-SPLF-1) to the inlet valve via PEEK tubing of 300  $\mu\text{m}$  internal diameter. From here, glass capillaries connected using PEEK fittings run through the shaft, into the tip of the holder, and lead the fluid into the liquid cell placed at the tip. In this study, by switching the flow between the inlet and outlet in a sequence, we could mix reagents in the field of view. The liquid 1 is introduced from the inlet side and withdrawn immediately as it enters the viewing area, which is continuously monitored under an optical microscope. However, a thin layer of liquid 1 adheres to the SiN window. At this stage, the holder is introduced into the column of the microscope. Then liquid 2 is introduced from the outlet side to initiate liquid mixing within the viewing area. By recording a STEM image series, the mixing process is captured in real-time. Before starting the experiment, the single tilt holder can be leak-tested in a dedicated station connected to a turbomolecular pump to mimic the vacuum inside the TEM. However, we leak-tested our liquid cell assembly in another microscope (JEOL JEM 2100) to ensure vacuum compatibility.

All the liquid cell experiments were carried out on a JEM-F200 multipurpose analytical S/TEM equipped with a cold field emission gun operated at 200 kV. The low-dose 4D-STEM measurements were performed on a TESCAN TENSOR 4D STEM operated at 100 kV and equipped with a DECTRIS QUADRO detector.

The molecule R-BINOL-CN was synthesised via Suzuki coupling by reacting 4-cyano phenyl boronic acid with 6,6'-dibromo-2,2'-diethoxy-1,1'-binaphthalene, as a white solid. A detailed account of the material synthesis, experimental methods and data analysis is provided in the supplementary information.

## Data availability

The data that support the findings of this study are openly available here: <https://figshare.com/s/ecdb48eaf24e3271338f>.

Received: 17 October 2024; Accepted: 2 January 2025;

Published online: 09 January 2025

## References

- Williamson, M. J., Tromp, R. M., Vereecken, P. M., Hull, R. & Ross, F. M. Dynamic microscopy of nanoscale cluster growth at the solid-liquid interface. *Nat. Mater.* **2**, 532–536 (2003).
- Haimei, Z. et al. Observation of single colloidal platinum nanocrystal growth trajectories. *Science* **324**, 1309–1312 (2009).
- Ross, F. M. Opportunities and challenges in liquid cell electron microscopy. *Science* **350**, aaa9886 (2015).
- Mirabello, G. et al. Crystallization by particle attachment is a colloidal assembly process. *Nat. Mater.* **19**, 391–396 (2020).
- Ou, Z., Wang, Z., Luo, B., Luijten, E. & Chen, Q. Kinetic pathways of crystallization at the nanoscale. *Nat. Mater.* **19**, 450–455 (2020).
- Liao, H.-G. et al. Facet development during platinum nanocube growth. *Science* **345**, 916–919 (2014).
- Ross, F. *Liquid Cell Electron Microscopy*. (Cambridge University Press, 2016).
- De Jonge, N. & Ross, F. M. Electron microscopy of specimens in liquid. *Nat. Nanotechnol.* **6**, 695–704 (2011).
- Nielsen, M. H., Aloni, S. & De Yoreo, J. J. In situ TEM imaging of CaCO<sub>3</sub> nucleation reveals coexistence of direct and indirect pathways. *Science* **345**, 1158–1162 (2014).
- Kelly, D. J. et al. In situ TEM imaging of solution-phase chemical reactions using 2D-heterostructure mixing cells. *Adv. Mater.* **33**, 2100668 (2021).
- Ianiro, A. et al. Liquid-liquid phase separation during amphiphilic self-assembly. *Nat. Chem.* **11**, 320–328 (2019).
- Kunnas, P., Moradi, M. A., Sommerdijk, N. & de Jonge, N. Strategy for optimizing experimental settings for studying low atomic number colloidal assemblies using liquid phase scanning transmission electron microscopy. *Ultramicroscopy* **240**, 113596 (2022).
- Rizvi, A., Mulvey, J. T. & Patterson, J. P. Observation of liquid-liquid-phase separation and vesicle spreading during supported bilayer formation via liquid-phase transmission electron microscopy. *Nano Lett.* **21**, 10325–10332 (2021).
- Patterson, J. P. et al. Observing the growth of metal-organic frameworks by in situ liquid cell transmission electron microscopy. *J. Am. Chem. Soc.* **137**, 7322–7328 (2015).
- Parent, L. R. et al. Directly observing micelle fusion and growth in solution by liquid-cell transmission electron microscopy. *J. Am. Chem. Soc.* **139**, 17140–17151 (2017).
- Yamazaki, T. et al. Two types of amorphous protein particles facilitate crystal nucleation. *Proc. Natl Acad. Sci. USA* **114**, 2154–2159 (2017).
- De Yoreo, J. J. & Sommerdijk, N. A. J. M. Investigating materials formation with liquid-phase and cryogenic TEM. *Nat. Rev. Mater.* **1**, 16035 (2016).
- Viçosa, A., Letourneau, J. J., Espitalier, F. & Inês Ré, M. An innovative antisolvent precipitation process as a promising technique to prepare ultrafine rifampicin particles. *J. Cryst. Growth* **342**, 80–87 (2012).
- Zhang, H. X. et al. Micronization of atorvastatin calcium by antisolvent precipitation process. *Int. J. Pharm.* **374**, 106–113 (2009).
- Matteucci, M. E., Hotze, M. A., Johnston, K. P. & Williams, R. O. Drug nanoparticles by antisolvent precipitation: Mixing energy versus surfactant stabilization. *Langmuir* **22**, 8951–8959 (2006).
- Yamazaki, T. & Kimura, Y. Radiolysis-induced crystallization of sodium chloride in acetone by electron beam irradiation. *Microsc. Microanal.* **27**, 459–465 (2021).
- Agranat, I., Caner, H. & Caldwell, J. Putting chirality to work: The strategy of chiral switches. *Nat. Rev. Drug Discov.* **1**, 753–768 (2002).
- Borowiecki, P. Enantiodifferentiation of promethazine using (S)-(-)-BINOL as the NMR chiral solvating agent: Determination of the enantiomeric purity and performance comparison with traditional chiral HPLC. *Tetrahedron Asymmetry* **26**, 16–23 (2015).
- Yuste, F., Sánchez-Obregón, R., Díaz, E. & García-Carrillo, M. A. Enantiodifferentiation of the antitumor alkaloid crispine A using the

- NMR chiral solvating agents (R)- and (S)-BINOL. *Tetrahedron Asymmetry* **25**, 224–228 (2014).
25. Yi, J. et al. Chiral discrimination of natural isoflavanones using (R)- and (S)-BINOL as the NMR chiral solvating agents. *Tetrahedron Asymmetry* **27**, 1153–1159 (2016).
26. Dighe, A. V., Podupu, P. K. R., Coliaie, P. & Singh, M. R. Three-step mechanism of antisolvent crystallization. *Cryst. Growth Des.* **22**, 3119–3127 (2022).
27. Dukes, M. J., Peckys, D. B. & De Jonge, N. Correlative fluorescence microscopy and scanning transmission electron microscopy of quantum-dot-labeled proteins in whole cells in liquid. *ACS Nano* **4**, 4110–4116 (2010).
28. Wu, H. et al. Mapping and controlling liquid layer thickness in liquid-phase (scanning) transmission electron microscopy. *Small Methods* **5**, 2001287 (2021).
29. White, E. R., Mecklenburg, M., Shevitski, B., Singer, S. B. & Regan, B. C. Charged nanoparticle dynamics in water induced by scanning transmission electron microscopy. *Langmuir* **28**, 3695–3698 (2012).
30. Merkens, S. et al. Quantification of reagent mixing in liquid flow cells for Liquid Phase-TEM. *Ultramicroscopy* **245**, 113654 (2023).
31. Yan, F. et al. Controlled synthesis of highly-branched plasmonic gold nanoparticles through peptoid engineering. *Nat. Commun.* **9**, 2327 (2018).
32. De Pace, C. et al. Imaging protein conformational space in liquid water. <https://doi.org/10.1101/2021.04.30.442083>.
33. Marchello, G. et al. 4D imaging of soft matter in liquid water. <https://doi.org/10.1101/2021.01.21.427613>.
34. Cookman, J., Hamilton, V., Price, L. S., Hall, S. R. & Bangert, U. Visualising early-stage liquid phase organic crystal growth: Via liquid cell electron microscopy. *Nanoscale* **12**, 4636–4644 (2020).
35. Merkens, S. et al. Toward sub-second solution exchange dynamics in flow reactors for liquid-phase transmission electron microscopy. *Nat. Commun.* **15**, 2522 (2024).
36. Smeets, P. J. M., Cho, K. R., Kempen, R. G. E., Sommerdijk, N. A. J. M. & De Yoreo, J. J. Calcium carbonate nucleation driven by ion binding in a biomimetic matrix revealed by in situ electron microscopy. *Nat. Mater.* **14**, 394–399 (2015).
37. Insight Chips. <https://www.insightchips.com/contact> (2023).
38. Van Omme, J. T. et al. Liquid phase transmission electron microscopy with flow and temperature control. *J. Mater. Chem. C Mater.* **8**, 10781–10790 (2020).
39. Groves, T. thick specimens in the cem and stem. resolution and image formation. *Ultramicroscopy* **1**, 15–31 (1975).
40. Wolf, S. G., Shimoni, E., Elbaum, M. & Houben, L. STEM tomography in biology. In 33–60. [https://doi.org/10.1007/978-3-319-68997-5\\_2](https://doi.org/10.1007/978-3-319-68997-5_2). (2018)
41. Sousa, A. A., Hohmann-Marriott, M. F., Zhang, G. & Leapman, R. D. Monte Carlo electron-trajectory simulations in bright-field and dark-field STEM: Implications for tomography of thick biological sections. *Ultramicroscopy* **109**, 213–221 (2009).
42. Abellan, P. et al. Factors influencing quantitative liquid (scanning) transmission electron microscopy. *Chem. Commun.* **50**, 4873–4880 (2014).
43. Takiyama, H. Morphology of NaCl crystals in drowning-out precipitation operation. *Chem. Eng. Res. Des.* **76**, 809–814 (1998).
44. Thanh, N. T. K., Maclean, N. & Mahiddine, S. Mechanisms of nucleation and growth of nanoparticles in solution. *Chem. Rev.* **114**, 7610–7630 (2014).
45. Dalmaschio, C. J., Ribeiro, C. & Leite, E. R. Impact of the colloidal state on the oriented attachment growth mechanism. *Nanoscale* **2**, 2336–2345 (2010).
46. Halder, A. & Ravishankar, N. Ultrafine single-crystalline gold nanowire arrays by oriented attachment. *Adv. Mater.* **19**, 1854–1858 (2007).
47. Zhang, Q. et al. Nearly monodisperse tungstate MWO<sub>4</sub> microspheres (M = Pb, Ca): Surfactant-assisted solution synthesis and optical properties. *Cryst. Growth Des.* **7**, 1423–1431 (2007).
48. Liu, B. et al. Morphology control of stolzite microcrystals with high hierarchy in solution. *Angew. Chem. - Int. Ed.* **43**, 4745–4750 (2004).
49. Liu, B. et al. Nanorod-direct oriented attachment growth and promoted crystallization processes evidenced in case of ZnWO<sub>4</sub>. *J. Phys. Chem. B* **108**, 2788–2792 (2004).
50. Muthukumar, M., Ober, C. K. & Thomas, E. L. Competing interactions and levels of ordering in self-organizing polymeric materials. *Science* **277**, 1225–1232 (1997).
51. Rosler, A., Vandermeulen, G. W. M. & Klok, A. Advanced drug delivery devices via self-assembly of amphiphilic block copolymers. *Adv. Drug Deliv. Rev.* vol. 53 [www.elsevier.com/locate/drugdeliv](http://www.elsevier.com/locate/drugdeliv) (2001).
52. MacFarlane, L., Zhao, C., Cai, J., Qiu, H. & Manners, I. Emerging applications for living crystallization-driven self-assembly. *Chem. Sci.* **12**, 4661–4682 (2021).
53. Frank, K. et al. Antisolvent controls the shape and size of anisotropic lead halide perovskite nanocrystals. *Nat. Commun.* **15**, 8952 (2024).
54. Wang, C., Wang, Z. & Zhang, X. Amphiphilic building blocks for self-assembly: from amphiphiles to supra-amphiphiles. *Acc. Chem. Res.* **45**, 608–618 (2012).
55. Malik, T., Stillhoff, E. C., Larsen, M. S., Yesibolati, M. N. & Mølhave, K. Mixing and flow control of liquids in nanochannel liquid phase electron microscopy. *Microsc. Microanal.* **27**, 99–100 (2021).

## Acknowledgements

We thank S. Vaidya of Samar Instruments, R. Ender and H. P. Garza of DENSsolutions for providing the DENSsolution Stream system used in this work. We thank P. Rama and S. Duraiswamy for providing auxiliary parts for interfacing the liquid holder with a syringe pump. We also thank P.H. Lu for help with 4D-STEM data collection. We thank P.V. Chaitanya for helping with XRD data acquisition. S.R.K.M. acknowledges funding from SPARC project –2434, through which this collaborative research work was carried out. Also, partial financial support from his SERB-ECR grant ECR/2017/002628, DRDO project (DRDO/DFTM/05/3424/AMP/008/M/01/IITHRC-013), JICA friendship project and IIT Hyderabad in establishing the research facilities to execute this study.

## Author contributions

S.R.K.M. conceived the concept of imaging while mixing two liquids in the DENSsolutions Stream system. S.R.K.M. and R.D.-B. supervised the project. G.U. and S.R.K.M. optimised experimental parameters and performed all the liquid cell experiments with the Stream system. R.J. synthesised the R-BINOL-CN molecule. Statistics from the STEM time series were extracted using PYTHON by J.P. and S.B. Preliminary liquid cell experiments using DENSsolutions Ocean system and selected area diffraction were performed by A.H.T. and S.R.K.M. 4D-STEM data acquisition and proof of concept analysis was done by R.H. 4D-STEM analysis and interpretation was done by S.D.-G. and S.R.K.M. Initial demonstration and setting up of the Steam system was done by H.S. and H.H.P.G. The manuscript was written by G.U. with inputs from all the authors. R.-A.E. reviewed the original manuscript. R.D.-B. and S.R.K.M. revised the final manuscript.

## Competing interests

The authors declare no competing interests.

### Additional information

**Supplementary information** The online version contains supplementary material available at <https://doi.org/10.1038/s42004-025-01407-3>.

**Correspondence** and requests for materials should be addressed to Rafal E. Dunin-Borkowski or Sai Rama Krishna Malladi.

**Peer review information** *Communications Chemistry* thanks Yuki Kimura and the other, anonymous, reviewer for their contribution to the peer review of this work. A peer review file is available.

**Reprints and permissions information** is available at <http://www.nature.com/reprints>

**Publisher's note** Springer Nature remains neutral with regard to jurisdictional claims in published maps and institutional affiliations.

**Open Access** This article is licensed under a Creative Commons Attribution-NonCommercial-NoDerivatives 4.0 International License, which permits any non-commercial use, sharing, distribution and reproduction in any medium or format, as long as you give appropriate credit to the original author(s) and the source, provide a link to the Creative Commons licence, and indicate if you modified the licensed material. You do not have permission under this licence to share adapted material derived from this article or parts of it. The images or other third party material in this article are included in the article's Creative Commons licence, unless indicated otherwise in a credit line to the material. If material is not included in the article's Creative Commons licence and your intended use is not permitted by statutory regulation or exceeds the permitted use, you will need to obtain permission directly from the copyright holder. To view a copy of this licence, visit <http://creativecommons.org/licenses/by-nc-nd/4.0/>.

© The Author(s) 2025